

Coherent Control of Bloch Oscillations in a Superconducting Circuit

Pengtao Song^{1,2,3,*} Zhongcheng Xiang^{1,4,†} Yu-Xiang Zhang¹ Zhan Wang^{1,3} Xueyi Guo¹,
Xinhui Ruan^{1,5} Xiaohui Song^{1,4} Kai Xu^{1,4} Yvonne Y. Gao,² Heng Fan^{1,3,4} and
Dongning Zheng^{1,3,4,‡}


¹*Institute of Physics, Chinese Academy of Sciences, Beijing 100190, China*

²*Centre for Quantum Technologies, National University of Singapore, Singapore 117543*

³*School of Physical Sciences, University of Chinese Academy of Sciences, Beijing 100190, China*

⁴*Hefei National Laboratory, Hefei 230088, China*

⁵*Department of Automation, Tsinghua University, Beijing 100084, China*

 (Received 1 January 2024; revised 25 February 2024; accepted 6 March 2024; published 3 April 2024)

Bloch oscillations (BOs) are oscillations of electrons under external constant forces in a lattice, revealing the wavelike behavior of electrons. BOs lead to the localization of the wave packet that is called Wannier-Stark localization (WSL), resulting in the inhibition of conductivity. We simulate BOs experimentally in a one-dimensional superconducting circuit with nine qubits. The nine qubits form a one-dimensional lattice and an electron is mapped to a photon. We experimentally realize the coherent control of BOs by applying a well-controlled driving force with a frequency close to BOs. We observe the competition between localization and delocalization of the wave packet by changing the drive parameters. Our study demonstrates the visualized wave behavior of electrons and proves a way to modulate electron transport in a perfect lattice.

DOI: [10.1103/PRXQuantum.5.020302](https://doi.org/10.1103/PRXQuantum.5.020302)

I. INTRODUCTION

It is well known that an electron in a periodic lattice propagates freely, following the seminal Bloch's theorem. A constant force will not speed up the propagation as one may naively expect but will make the electron oscillate locally *in situ*. The oscillation results in the localization of the electron wave function and, thus, the breakdown of the transport. Such oscillation and localization, known as Bloch oscillation (BO) and Wannier-Stark localization (WSL) were first studied about a century ago by Bloch and Zener [1,2] and by Wannier in the 1960s [3]. However, due to the defects and dissipations in real-life crystals, the observation of BOs was not achieved until the experiments on semiconductor superlattices in the 1990s [4,5]. Since then, BOs have also been observed in Bose-Einstein condensates [6–8], optical waveguide arrays [9], and superconducting circuits [10].

The amplitude of the BO, viewed as a quantification of the WSL, can be tuned to be much larger by applying periodic driving on top of the constant force, giving rise to the so-called super-Bloch oscillations (SBOs) [11]. This effect can be used as a control knob for the turning on or off of transportation. It has triggered many ongoing research works on the subject of BOs and SBOs in both theory [12–18] and experiment [7,11,19–21].

Superconducting circuits [22,23], with which many significant studies of quantum computing and information have been achieved [24–27], offer a promising platform for quantum simulations in condensed-matter physics, due to their excellent scalability, editable Hamiltonian, and precise controllability. Unsymmetrical BOs and WSLs have been demonstrated in superconducting circuits [10]; however, the coherent control of BOs remains a subject of ongoing studies. We realize symmetrical BOs and the coherent control of BOs by applying a driving. We observe the competition between BO and SBOs by changing the phase and amplitude of the driving. The BOs are simulated experimentally by using an array of nine superconducting qubits. With precise on-site control of the qubit frequencies in the time domain, a constant force and a driving are realized to manipulate the wave packet of the photon. We observe the delocalization of the wave packet with resonant driving due to assisted tunneling between the Wannier-Stark levels. Additionally, we

*ptsong@nus.edu.sg

†zcxiang@iphy.ac.cn

‡dzheng@iphy.ac.cn

Published by the American Physical Society under the terms of the [Creative Commons Attribution 4.0 International](https://creativecommons.org/licenses/by/4.0/) license. Further distribution of this work must maintain attribution to the author(s) and the published article's title, journal citation, and DOI.

observe more localization with a detuned driving with a specific amplitude and phase, which exhibits quantum interference between the wave of BOs and the driving wave.

II. SYSTEM HAMILTONIAN AND SIMULATION DESIGN

We perform our experiment on a superconducting chip in a dilution refrigerator with a base temperature of about 15 mK. The chip contains ten transmon qubits [28,29], labeled as Q_0 to Q_9 on the chip [see Fig. 1(a)], and each qubit has its own readout cavity and XY and Z control lines. All the readout cavities are coupled to a readout line for multiplexed readout [30]. To maintain the parity symmetry with respect to a central qubit, we utilize only nine of them (from Q_1 to Q_9) for the coherent control experiment of BOs.

Within the computation space, the Hamiltonian of the nine-qubit system reads [31]

$$\hat{H} = \sum_{j=1}^8 g_{j,j+1} (\hat{\sigma}_j^+ \hat{\sigma}_{j+1}^- + \hat{\sigma}_{j+1}^+ \hat{\sigma}_j^-) + \sum_{j=1}^9 \omega_j \hat{\sigma}_j^+ \hat{\sigma}_j^-, \quad (1)$$

where $\hat{\sigma}_j^+$ and $\hat{\sigma}_j^-$ denote the creation and annihilation operators of Q_j , respectively, $g_{j,j+1}/2\pi \approx 25$ MHz is the coupling strength between Q_j and Q_{j+1} , and ω_j is the transition frequency of Q_j .

In order to observe SBOs, an experimental configuration, shown in Fig. 1(b), is required. To realize it, we linearly detune the frequencies of the nine qubits by a gradient of F , i.e., $\omega_j - \omega_{j+1} = F$. Then, we modulate the qubits to make each ω_j oscillate in time with the same frequency F_D but with different amplitudes. The amplitudes increase linearly with respect to the distance from

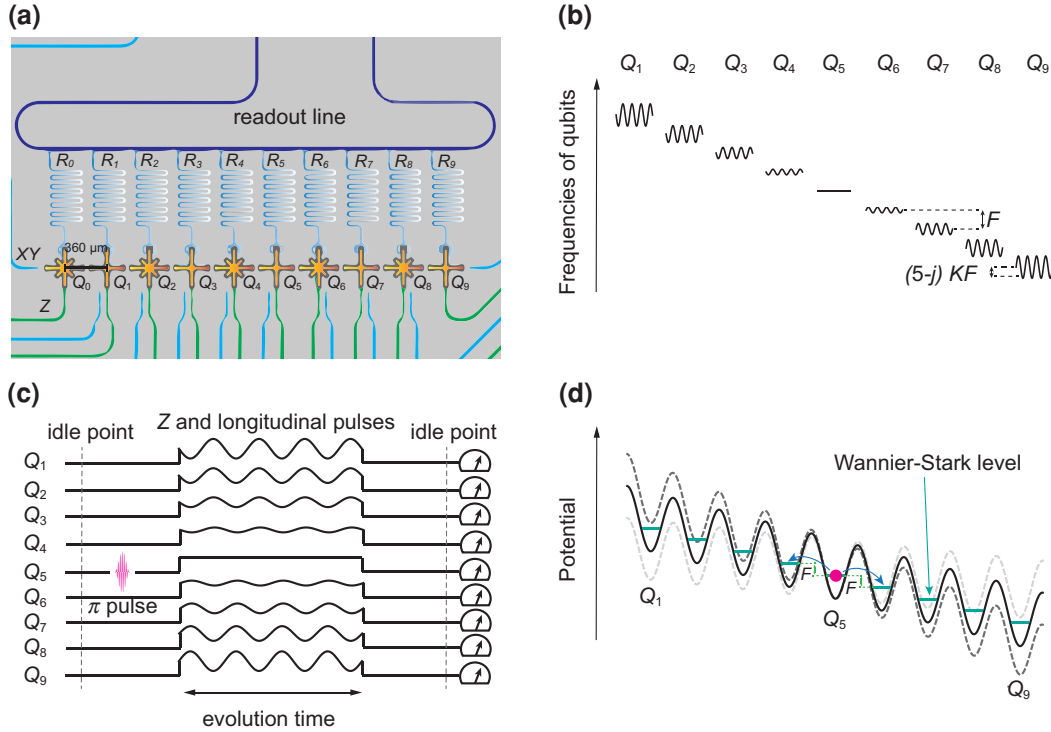


FIG. 1. The schematic diagram for realizing driving-controlled Bloch oscillations on a ten-qubit chip. (a) A drawing of the ten-qubit chip. The qubits form a one-dimensional chain, while the even-numbered (or odd-numbered) qubits have the same geometry. Each qubit has an independent readout cavity and two local control lines for universal control. The frequencies of the qubits can be tuned by applying ac fields or dc currents through the Z control lines. In this paper, we do not use Q_0 , by tuning its frequency far away from those of the other qubits. (b) The frequency arrangement of the nine qubits. The base frequencies of the nine qubits decrease linearly with a gradient of F , while a harmonic oscillation is added to the base frequency for each qubit. The amplitude of the harmonic oscillation is $(5-j)KF$, where j is the qubit number and K is the amplitude coefficient. (c) The pulse sequences of the nine qubits for realizing driving-controlled BOs. For preparing the idle point, there is a large enough detuning between every two qubits to guarantee the weak-coupling regime. The initial single-photon state is generated by applying a π pulse to Q_5 . The frequency arrangement of the qubits as shown in (b) is achieved by applying Z and longitudinal control pulses to qubits. (d) An equivalent Bose-Hubbard model with a time-dependent potential for describing the frequency arrangement of the qubits in (b). The red dot in the Q_5 site represents a photon that can tunnel to the Q_4 site or the Q_6 site.

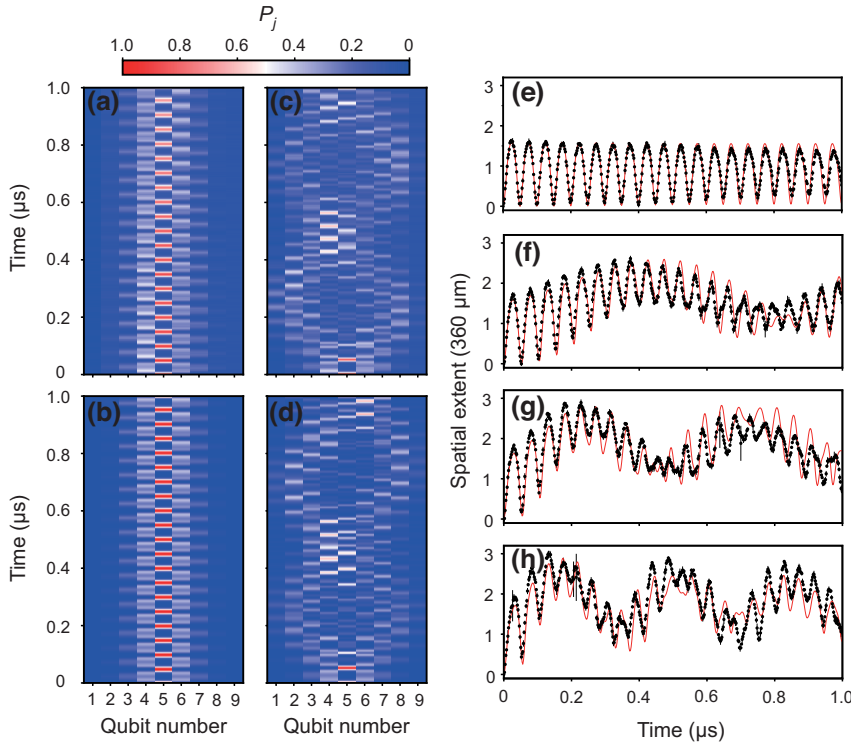


FIG. 2. Delocalizing Bloch oscillations in position space. (a),(b) Bloch oscillations (a) in experiment and (b) in theory, when the equivalent force $F/2\pi$ is 20 MHz and the amplitude coefficient K is zero. We excite Q_5 and then capture the time evolution of the state projection on the σ_Z axis of each qubit. (c),(d) Bloch oscillations under resonant driving (c) in experiment and (d) in theory, when $F_D/2\pi = 20$ MHz and $K = 0.2$. (e)–(h) The time-domain oscillations with different amplitude coefficients: (e) $K = 0$; (f) $K = 0.1$; (g) $K = 0.2$; (h) $K = 0.3$. The spatial extent is defined as $E_s(t) = \sum_{j=1}^9 P_j(t)|j - 5|d$, where $d = 360 \mu\text{m}$ is the physical distance between the two nearest qubits. The black data points represent the experimental data, while the solid red lines correspond to the theoretical simulations.

the central qubit with a gradient of KF (for the observation of BOs, we just need to set $K = 0$). This modulation of each ω_j is realized by a low-frequency (5–20 MHz for this experiment) pulse through the Z control lines [32–34]. Now, the system is described by the following time-dependent Hamiltonian:

$$\hat{H}_{\text{SBOs}} = \sum_{j=1}^8 g_{j,j+1}(\hat{\sigma}_j^+ \hat{\sigma}_{j+1}^- + \hat{\sigma}_{j+1}^+ \hat{\sigma}_j^-) + \sum_{j=1}^9 (5-j)(F + KF \cos(F_D t + \varphi)) \hat{\sigma}_j^+ \hat{\sigma}_j^-, \quad (2)$$

where φ denotes the initial phase of the drivings. We can coherently control the dynamics by tuning K , F_D , and φ . This Hamiltonian simulates a Bose-Hubbard model for hard-core bosons in a time-dependent potential, which is illustrated in Fig. 1(d).

III. SIMULATION OF BLOCH OSCILLATIONS UNDER DRIVING

We study the propagation of a single excitation initialized at the central qubit Q_5 to simulate the action of a single electron in a periodic lattice. This initial state is prepared by tuning the nine qubits far off resonance from each other at first—to the idle point of the setup where no tunneling occurs—followed by pumping Q_5 to its first

excited state. Then, the system is turned away from the idle point by sending the control pulses belonging to the configuration sketched in Fig. 1(b). The qubits evolve according to the Hamiltonian in Eq. (2). The duration of the evolution is controlled by the pulse lengths. After that, we decouple all the qubits (back to the idle point) and read out the population on the excited state (P_j) for every qubit (Q_j).

In our experiment, at first, we set the external force $F = 0$ and find that the wave packet of the photon will propagate toward the chain ends (Q_1 , Q_9) and then be reflected back to the chain center (see Appendix B). This means that if the external force is zero and the lattice is infinite, an electron will spread freely. If we set an external force of $F/2\pi = 20$ MHz ($K = 0$), as shown in Figs. 2(a) and 2(b), the wave packet of the photon oscillates around Q_5 with an amplitude that is too small to reach the chain ends (Q_1 and Q_9). This is because the external constant force generates Wannier-Stark levels, which break the resonance between neighboring sites and hence suppress the site-to-site tunneling, giving rise to the phenomenon of Wannier-Stark localization. This simulates the BOs of electrons in a periodic lattice with constant force.

Next, we show that the Wannier-Stark localization can be turned off by adding longitudinal control fields to every qubit. Here, we set $K = 0.2$ and $F_D = 20$ MHz and we illustrate the results in Figs. 2(c) and 2(d). We observe, in addition to the quick and localized oscillations, a mode of oscillation with a larger amplitude and a lower frequency. This is because the longitudinal control introduces a series of sidebands to every qubit and the energy gaps between

the sidebands are F_D . In the case of $F = F_D$, the resonance between neighboring qubits is restored by these sidebands, so that the site-to-site tunneling is activated. Then, the wave packet of the photon is delocalized and keeps spreading until it is reflected by the chain ends (Q_1 and Q_9), resulting in a slower oscillation mode. The frequency of this mode is proportional to the tunneling rate between the Wannier-Stark levels.

To quantitatively analyze the oscillation seen from Fig. 2(c), we define the spatial extent [19] of the single-photon wave packet as

$$E_s(t) = \sum_{j=1}^9 P_j(t) |j - 5\rangle, \quad (3)$$

where $d = 360 \mu\text{m}$ is the physical distance between two nearest-neighbor qubits. The spatial extents are plotted as a function of time in Figs. 2(e)–2(h). This shows that, without longitudinal drivings ($K = 0$), only fast oscillation is observed (with the frequency $F/2\pi$). With resonant driving ($K \neq 0$), both the fast and the slow oscillations become evident. One can see by comparing Figs. 2(f)–2(h), or directly from Fig. 3(b), that the frequency of the slow mode increases linearly with the driving amplitude K . The increased frequency of the slow mode can be attributed to the increased tunneling rate between the Wannier-Stark levels. This means that in an infinite lattice in the presence of Wannier-Stark localization, one can restore the electron transportation using an additional on-site harmonic driving with $F_D = F$ and control its mobility by means of the driving amplitude K .

We convert $E_s(t)$ from the time domain to the frequency domain using a fast Fourier transform (FFT) and plot the results in Fig. 3(a). This shows that the frequency of the fast mode is just the frequency of the BOs, while the low-frequency component is the beat frequency between the BOs and the driving (only for detuned driving $F_D \neq F$). We also define the average amplitude of the oscillation as

$$A = \frac{\int_0^{t_0} E_s(t) dt}{t_0} = \frac{\int_0^{t_0} \left(\sum_{j=1}^9 P_j(t) |j - 5\rangle \right) dt}{t_0}, \quad (4)$$

which is a time-domain average of the spatial extent, where t_0 is the evolution time. Considering the decoherence of the qubits and the stability of the experiment, we take $t_0 = 1 \mu\text{s}$. We can also obtain the beat frequency by taking the low-frequency component after the FFT. The average amplitudes and beat frequencies of the oscillations with different driving amplitudes (K), driving detunings ($F_D - F$), and initial driving phases (φ) are shown in Figs. 3(b)–3(d).

When increasing the driving amplitude (K), both the average amplitude and the low-frequency component of the oscillation will increase. The limitation of the average

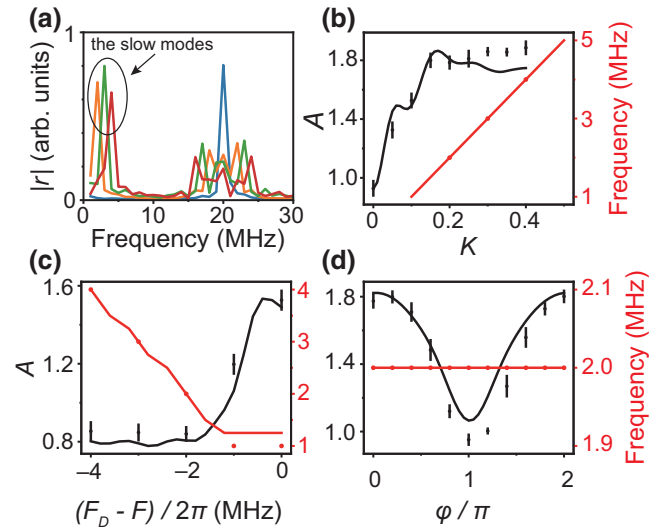


FIG. 3. The average amplitudes of the BOs and the frequencies of the slow modes with different drive amplitudes, detunings, and phases. (a) The oscillations in the frequency domain. The frequency-domain data are transformed from the time-domain data in Figs. 2(e)–2(f), with $K = 0$ (blue line), $K = 0.2$ (orange line), $K = 0.3$ (green line), and $K = 0.4$ (red line) by a fast Fourier transform (FFT). The high-frequency peaks belong to the original BOs and we take the low-frequency peaks as the beat frequency. (b)–(d) The average amplitudes and beat frequencies of the oscillations versus (b) the driving amplitude K , (c) the drive detuning $(F_D - F)/2\pi$, and (d) the drive phase φ , respectively, with $F/2\pi = 20 \text{ MHz}$, where $F_D/2\pi = 20 \text{ MHz}$ and $\varphi = 0$ in (b), $K = 0.3$ and $\varphi = 0$ in (c), and $F_D/2\pi = 22 \text{ MHz}$ and $K = 0.15$ in (d). The dots represent the experimental data and the lines represent the corresponding simulation results.

amplitude is due to the qubit numbers. Clearly, the average amplitudes of the oscillations with resonant driving are larger than without driving, which quantitatively demonstrates the delocalization of the wave packet. With detuned driving, when the detuning $(F_D - F)$ becomes larger, the average amplitudes of the oscillations will decrease and the low-frequency component is equal to the absolute value of the detuning $|F_D - F|$. The initial phase (φ) will not affect the low-frequency component but it can tune the average amplitudes of the oscillations periodically. In short, we can control the oscillation amplitude and frequency by changing the drive amplitude, the drive detuning, and the initial drive phase.

For further study, we calculate the differences of the average amplitudes of the oscillations with driving (A_w) and without driving ($A_{w/o}$). We set $F/2\pi = 20 \text{ MHz}$ and $F_D/2\pi = 18 \text{ MHz}$ and then measure the difference of the average amplitudes with changing the values of the drive amplitude (K) and the initial drive phase (φ). As shown in Fig. 4(a), with driving, the green region shows amplification of the average oscillation amplitude, while the purple region shows that the average oscillation amplitude

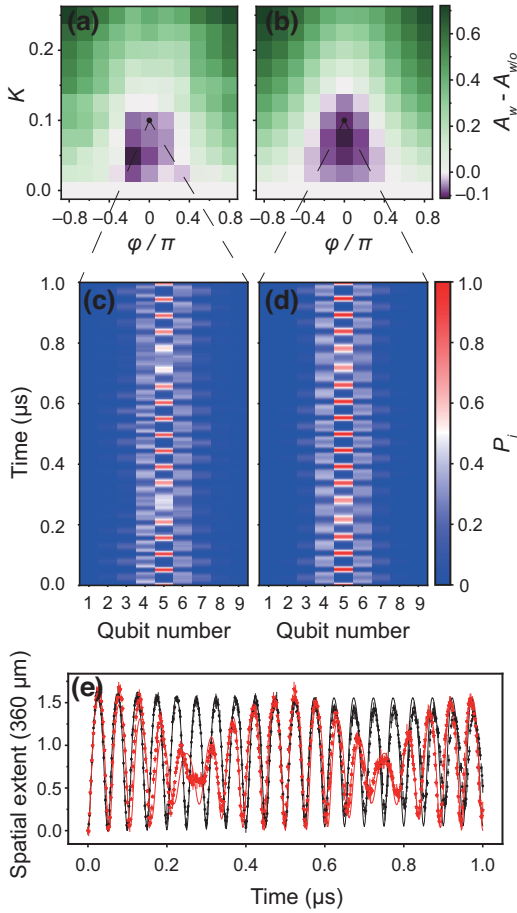


FIG. 4. Bloch oscillations under detuned driving. (a),(b) The differences of the average amplitude of oscillation with driving (A_w) and without driving ($A_{w/o}$) versus the drive amplitude K and the drive phase φ (a) in experiment and (b) in theory, where $F/2\pi = 20$ MHz and $F_D/2\pi = 18$ MHz. (c),(d) The time evolution of the wave packet with $K = 0.1$ in (a) and (b), respectively: (c) experiment; (d) theory. (e) A comparison of the spatial extent of the oscillations with and without driving in the time domain. The oscillations with driving in (c) (red stars) and (d) (solid red line), and the oscillation without driving (black stars, experiment; solid black line, theory).

can even be suppressed. The theoretical result is shown in Fig. 4(b), which matches the experimental result. This is a quantum interference phenomenon between the wave of the BOs and the beat-frequency wave. In Figs. 4(a) and 4(b), the green region represents the delocalized area, the purple region denotes the more localized area, while the white region signifies the critical line. The time-domain data of the wave packet and the spatial extent in the more localized area are shown in Figs. 4(c)–4(e). As shown in Fig. 4(e), we observe that the spatial extent of the oscillations is modulated by the driving and shows a more delocalizing behavior. This phenomenon means that with some specific parameters of the additional harmonic force,

the electrons can be more localized in the lattice than the BOs.

IV. CONCLUSIONS

In summary, we simulate the BOs of a single electron in a superconducting circuit by mapping the electron to a photon. We control the time evolution of the BOs using an external driving, which is realized by applying longitudinal control fields to the qubits. By changing the parameters of the driving, we investigate how the oscillation amplitude and frequency change. Under a resonant drive, the tunneling rate between the Wannier-Stark levels increases with an increase in the driving amplitude, leading to the delocalization of the wave packet. Under a detuned drive, a beat-frequency wave is generated, which interferes with the wave of the BOs. More localized oscillations are observed under detuned driving with specific amplitudes and phases by integrating the spatial extent of the wave packet in the time domain. Since the WSL is detrimental to electron transport, our study points out that one possible solution is to apply external driving to promote electron delocalization and indicates that the wave packet of electrons may become more localized with some drive parameters.

ACKNOWLEDGMENTS

This work was supported by the State Key Development Program for Basic Research of China (Grant No. 2017YFA0304300), the Key-Area Research and Development Program of Guangdong Province, China (Grant No. 2020B0303030001), the National Natural Science Foundation of China (Grant No. T2121001), and the Strategic Priority Research Program of the Chinese Academy of Sciences (Grant No. XDB28000000). Y.Y.G. and P.S. acknowledge funding support from National Research Foundation Singapore grant number NRF2020-NRF-ISF004-3540.

APPENDIX A: DEVICE DETAILS AND MEASUREMENT CALIBRATIONS

1. Fabrication

The chip has a four-layer structure. The layer of the Josephson junction is exposed using electron-beam lithography, while the other layers are exposed using optical-beam lithography. The first layer consists of the capacitance of transmons, readout cavities, control lines, and transmission lines and is made by evaporating a 100-nm aluminum film on the sapphire substrate and then etching the film using aluminum etchant. The second layer consists of the gold markers that are used for alignment during electron-beam lithography. The third layer is a Josephson-junction layer that is made by double-angle evaporation [35,36] (-60° for 65 nm and 0° for 100 nm). The final

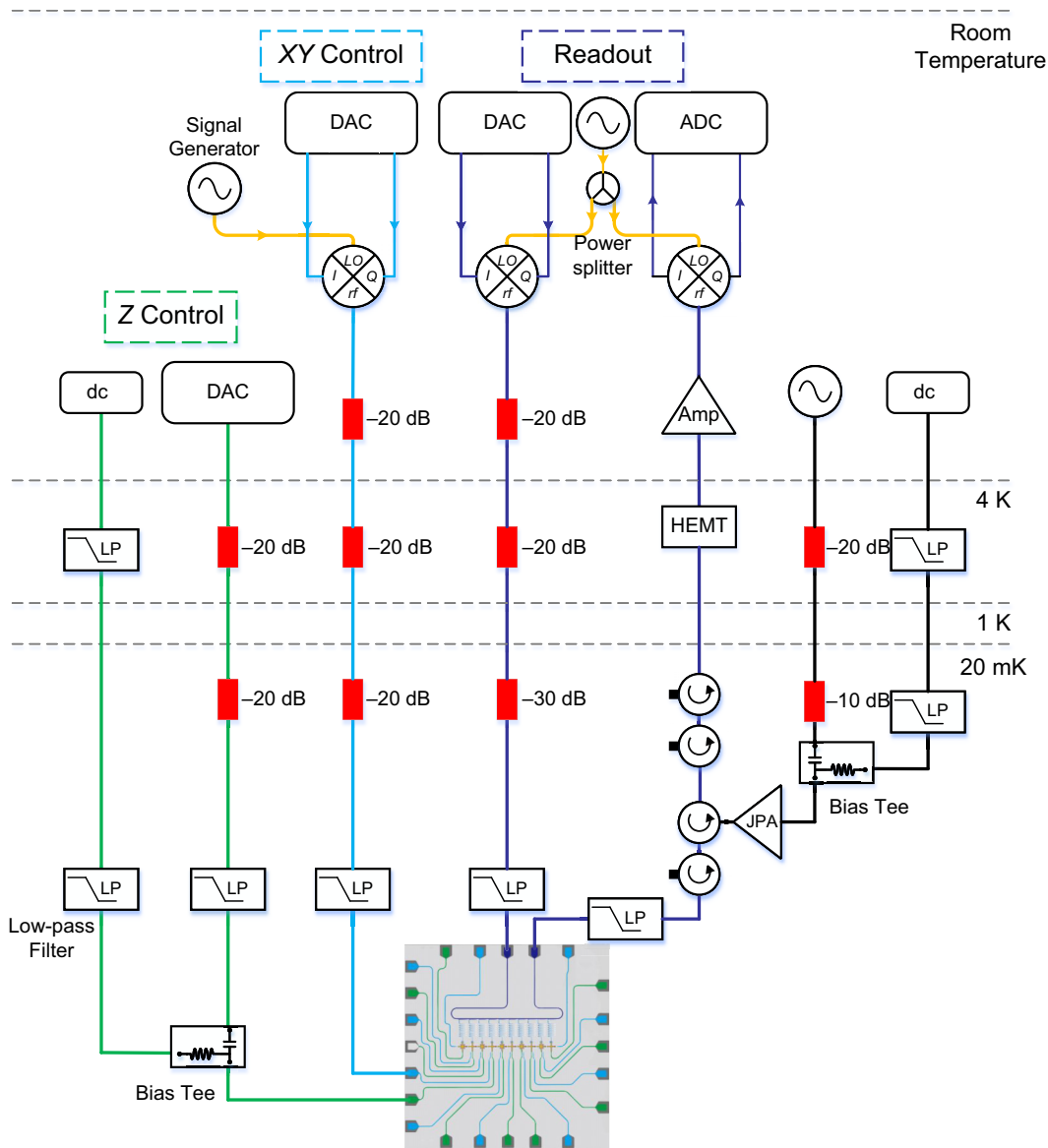


FIG. 5. The measurement setup. Each qubit has a XY control line and a Z control line. The XY control lines are used for exciting the qubits, while the Z control lines are used for dc biases and longitudinal controls. We use a standard heterodyne measurement to read out the qubits, where the Josephson parametric amplifier (JPA) is used for improving the visibility of the readout.

layer consists of the air bridges [37], which are used for reducing the crosstalk between different control lines.

2. Measurement setup

The chip is put into a dilution refrigerator with an environment temperature of about 15 mK to avoid thermal excitations and the measurement setup is shown in Fig. 5. The attenuators and filters are used for reducing noise. The digital-to-analog converter (DAC) is used for generating low-frequency signals (0–500 MHz), while the signal generator is used for generating high-frequency signals (1–8 GHz). For the Z control of the qubit, a bias tee combines the dc current and the low-frequency signals, where the

dc current is used for biasing the qubit to the idle point and the low-frequency signals are used for the Z pulse and the longitudinal control field. For the XY control of the qubit, the mixed signals after the I - Q mixer are used for exciting the qubit. Heterodyne detection is used for the multiplexed readout of the ten qubits and the output signals are acquired by an analog-to-digital converter (ADC). A Josephson parametric amplifier (JPA) is used for improving the visibility of the readout.

3. Device performance and basic settings

The basic parameters of the device are shown in Table I. The energy decoherence time T_{1i} of each qubit at the idle

TABLE I. The basic parameters of the device, where f_r is the frequency of the readout cavity, f_{qm} is the maximum frequency of the qubit, f_{qi} is the frequency of the qubit at the idle point, χ_i is the effective coupling between the readout cavity and the qubit when the qubit is at the idle point, α is the anharmonicity of the qubit, T_{1i} is the energy decoherence time of the qubit, T_{2i}^* is the Ramsey dephasing time of the qubit, T_{2i}^{echo} is the spin-echo dephasing time of the qubit, and F_g and F_e are the readout fidelity for the ground state and the excited state, respectively.

Parameters	Q_0	Q_1	Q_2	Q_3	Q_4	Q_5	Q_6	Q_7	Q_8	Q_9	Average
f_r (GHz)	6.514	6.54	6.553	6.575	6.592	6.614	6.633	6.651	6.67	6.69	...
f_{qm} (GHz)	5.22	5.55	5.21	5.6	5.16	5.7	5.18	5.66	5.14	5.66	...
f_{qi} (GHz)	5.037	5.534	4.929	5.59	5.063	5.694	5.003	5.45	5.049	5.572	...
$\chi_i/2\pi$ (MHz)	0.25	0.49	0.24	0.42	0.23	0.49	0.24	0.44	0.2	0.53	...
α (MHz)	200	260	200	260	200	250	200	260	200	260	...
T_{1i} (μs)	51.4	36.3	47.6	54.5	48.6	50	41	36.7	18	27.9	41.2
T_{2i}^* (μs)	1.7	2.6	0.8	7.3	3.9	2.1	2.8	2.1	2.1	3.2	2.9
T_{2i}^{echo} (μs)	8.1	11.7	6.4	36.4	26.6	12.9	21.2	13.2	20.2	18.4	17.5
F_g	0.945	0.962	0.968	0.988	0.978	0.99	0.976	0.993	0.95	0.981	0.973
F_e	0.89	0.871	0.93	0.868	0.903	0.877	0.862	0.919	0.885	0.921	0.893

point is greater than or equal to $18 \mu\text{s}$ and then the maximum evolution time in this paper is $1 \mu\text{s}$, so we can ignore the effect of decoherence on the experimental results. To make sure that the coupling strength between every two qubits is small enough at the idle point, we set the detuning between every two nearest-neighbor qubits to be greater than 400 MHz and we set the detuning between every two next-nearest-neighbor qubits to be greater than 40 MHz . The coupling strengths and effective coupling strengths at the idle point between the qubits are shown in Table II. We normalize the readout probability for every qubit by means of the matrix [31]

$$m = \begin{bmatrix} F_g & 1 - F_e \\ 1 - F_g & F_e \end{bmatrix},$$

where F_g and F_e are the readout fidelity of the ground state and the excited state, respectively.

4. Crosstalk and distortion calibrations of Z pulses

Since the layout of the qubit control lines is crowded, crosstalk is difficult to avoid. We measure the crosstalk between all the Z control lines of qubits and the crosstalk matrix M_Φ , which is shown in Table III with the matrix, where $\Phi_{\text{actual}} = M_\Phi \Phi_{\text{ideal}}$, in which Φ is the flux in the superconducting quantum interference device (SQUID)

TABLE II. The coupling strengths between the qubits. We only consider the nearest-neighbor coupling ($Q_{j,j+1}$) and the next-nearest-neighbor coupling ($Q_{j,j+2}$) between the qubits. The coupling strength g here is measured by the swap frequency when tuning the two qubits to the same frequency. The effective coupling strength g_i when all the qubits are at the idle point is calculated by $g_i = g^2/\Delta$, where Δ is the detuning between two qubits.

	Q_{0-1}	Q_{1-2}	Q_{2-3}	Q_{3-4}	Q_{4-5}	Q_{5-6}	Q_{6-7}	Q_{7-8}	Q_{8-9}	Q_{0-2}	Q_{1-3}	Q_{2-4}	Q_{3-5}	Q_{4-6}	Q_{5-7}	Q_{6-8}	Q_{7-9}
$g/2\pi$ (MHz)	12.05	12.2	11.9	11.9	11.9	11.76	11.9	12.05	12.35	1.1	0.69	1.1	0.69	1.1	0.61	1.1	0.71
$g_i/2\pi$ (MHz)	0.29	0.25	0.21	0.27	0.22	0.2	0.32	0.36	0.29	0.011	0.008	0.009	0.005	0.02	0.002	0.026	0.004

loop of the qubit [38]. Due to the presence of the air bridges on the control lines, the average value of the crosstalk-matrix elements (except for the diagonal elements) is 0.0032 . Therefore, all the amplitudes of the Z pulses set for the DACs can be calculated by $Z_{\text{set}} = M_\Phi^{-1} Z_{\text{actual}}$, where M_Φ^{-1} is the inverse matrix of M_Φ , Z_{set} is the amplitude of the Z pulse set for the DAC, and Z_{actual} is the actual observed amplitude of the qubit.

Because of the bandwidth limitation on the control circuits, even if we set a perfect square wave, the actual wave form seen by the qubit is distorted. We measure the actual wave form of the Z pulse seen by a qubit and calibrate the distortion [10].

5. Calibration of longitudinal control pulses

We expect the frequencies of the qubits to oscillate harmonically in the time domain; however, the relationship between the qubit frequency and the external flux is not linear [39], so a simple cosine wave added to a Z pulse cannot achieve the expected frequency oscillation in the time domain. We can expand the qubit frequency polynomially,

$$f(x) = \sum_{j=0}^{+\infty} a_j x^j, \quad (\text{A1})$$

TABLE III. The crosstalk matrix.

$M_\Phi =$	100	-0.32	1.12	0.31	0.12	0.64	0.33	0.37	0.27	0.34
	-0.23	100	-0.41	-0.33	0	-0.36	-0.20	-0.26	-0.21	-0.24
	-0.58	-0.38	100	-0.77	-0.05	-0.75	-0.50	-0.65	-0.52	-0.57
	-0.27	-0.68	-0.85	100	0	-0.29	-0.26	-0.31	-0.27	-0.28
	0.51	1.02	0.81	2.98	100	0.39	0.50	0.69	0.55	0.49
	0.32	0.61	0.40	0.90	-1.02	100	0.82	0.64	0.45	0.37
	-0.50	-0.85	-0.50	-0.98	6.1	1.88	100	-2.20	-1.03	-0.61
	-0.30	-0.49	-0.28	-0.53	0.28	0.52	0.10	100	-1.13	-0.42
	-0.46	-0.77	-0.38	-0.77	0.38	0.79	0.29	-0.15	100	-0.82
	0.31	0.45	0.24	0.48	-0.26	-0.53	-0.25	0.08	0.72	100

$\times 10^{-2}$

where x is the amplitude of the Z pulse and a_j is the corresponding coefficient. If we only consider the second-order expansion, the frequency of qubit can be written as

$$f(x) = ax^2 + bx + c, \quad (\text{A2})$$

where a , b , and c are the corresponding coefficients. If we set the longitudinal control pulse to

$$x = x_0 + \Delta x \cos(\omega t), \quad (\text{A3})$$

where x_0 is the constant component (common Z pulse), Δx is the amplitude of longitudinal control component. We can

then obtain

$$\begin{aligned} f(x) &= ax_0^2 + bx_0 + c + (2ax_0 + b)\Delta x \cos(\omega t) \\ &= f(x_0) + f'(x_0)\Delta x \cos(\omega t) \\ &\quad + a(\Delta x)^2/2 + (a(\Delta x)^2/2)\cos(2\omega t), \end{aligned} \quad (\text{A4})$$

where $f'(x) = 2ax + b$ is the derivative function of $f(x)$. The last two terms in Eq. (A4) are unexpected. To eliminate these two terms, we can set the longitudinal control pulse to

$$\begin{aligned} x_{\text{cali}} &= x_0 + \Delta x \cos(\omega t) - a(\Delta x)^2/(2f'(x_0)) \\ &\quad - a(\Delta x)^2 \cos(2\omega t)/(2f'(x_0)). \end{aligned} \quad (\text{A5})$$

As shown in Eq. (A5), we need to add an additional dc offset and a double frequency signal for calibration. The energy spectra of the qubits during the longitudinal control pulses before and after calibration are shown in Fig. 6.

APPENDIX B: QUANTUM WALKS AND BLOCH OSCILLATIONS

Before the BO experiment, we need to do some calibration step by step to build up the measurement conditions. The first calibration concerns quantum walks. We set the frequencies of the ten qubits to be equal and then measure the time evolution of the probability density of the photons after exciting one or two qubits, as shown in Fig. 7. This quantum-walk experiment indicates that the electrons can spread freely in a lattice. The second preexperiment concerns the BOs. When setting a nonzero frequency gradient F , we observe the localization of the probability of the photon. As shown in Fig. 8, with larger values of F , more localizations are observed. This BO experiment shows that an electron will be localized in the lattice, with a constant force is applied to the electron.

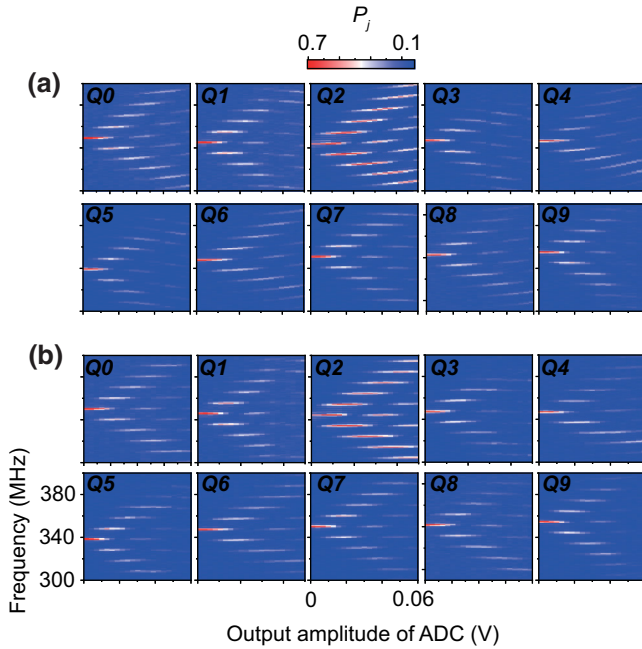


FIG. 6. The longitudinal control-field calibration. The qubit spectra under the longitudinal control field (a) before calibration and (b) after calibration. The qubit spectra are more aligned horizontally after calibration.

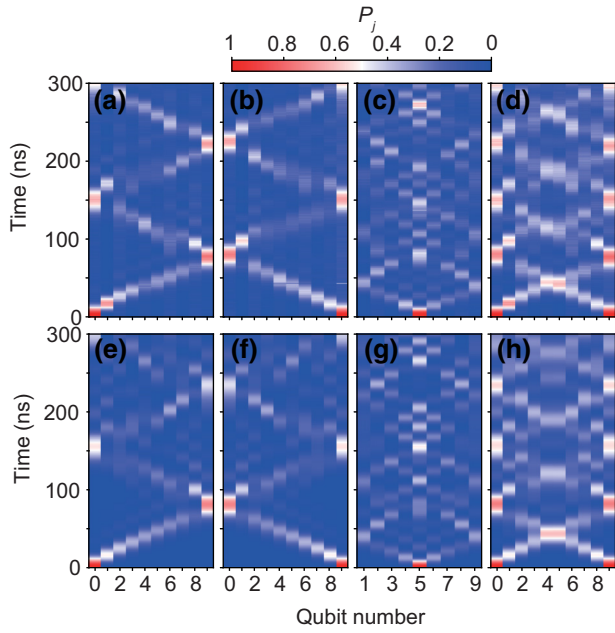


FIG. 7. Quantum walks. We tune the frequencies of the qubits to be the same and then excite one or two qubits and monitor the time evolution of the photon density distribution: (a)–(d) are experimental data, while (e)–(h) are the corresponding theoretical data. In (a) and (e), we excite Q_0 ; in (b) and (f), we excite Q_9 ; in (c) and (g), we excite Q_5 ; and in (d) and (h), we excite Q_0 and Q_9 .

APPENDIX C: THE COMPETITION BETWEEN LOCALIZATION AND DELOCALIZATION

As shown in Fig. 4, we have demonstrated the competition between localization and delocalization both in experiment and theory with a drive detuning $(F_D - F)/2\pi = -2$ MHz. Here, we show more theoretical results about the competition with various drive detunings in Fig. 9, and we can find that the location of more localized area (purple region) will shift with different detunings. As shown in Fig. 9(b), the more localized area with resonant drive ($F_D = F$) is much smaller than the detuned drive. This result indicates the resonant drive is easier to delocalize BOs by avoiding the more localized area.

APPENDIX D: THEORETICAL ANALYSIS

The Hamiltonian of the system with qubit anharmonicity is

$$H = g_0 \sum_j (\sigma_j^\dagger \sigma_{j+1} + \sigma_j^\dagger \sigma_{j-1}) + \sum_j \frac{U}{2} n_j (n_j - 1) + \sum_n nF [1 + K \cos(F_D t + \varphi)] \sigma_n^\dagger \sigma_n, \quad (\text{D1})$$

where $n_j = \sigma_j^\dagger \sigma_j$ is the number operator and $U = -\alpha$ is the qubit anharmonicity. In this paper, $g/\alpha \ll 1$ and

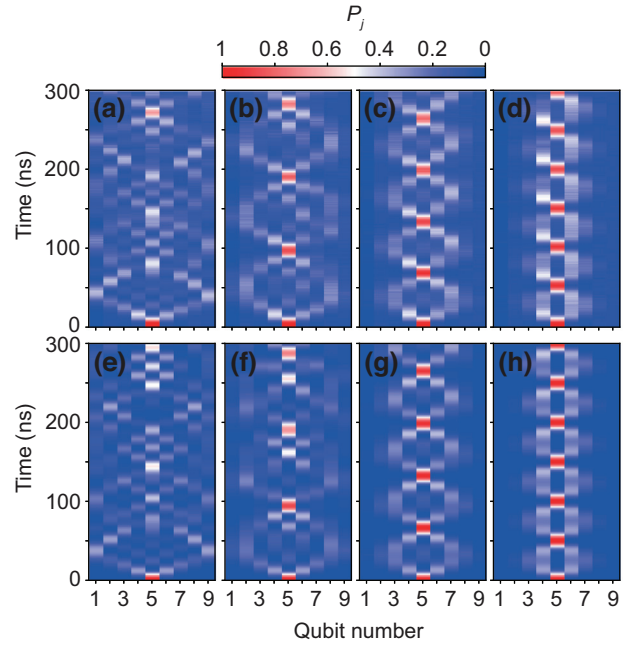


FIG. 8. Bloch oscillations: (a)–(d) are experimental data, while (e)–(h) are the corresponding theoretical data. The equivalent force is as follows: (a),(e) $F/2\pi = 0$ MHz; (b),(f) $F/2\pi = 10$ MHz; (c),(g) $F/2\pi = 15$ MHz; and (d),(h) $F/2\pi = 20$ MHz.

$F/\alpha \ll 1$ and the probability of higher-energy-level leakage is very low, thus enabling us to treat the qubits as an ideal two-level system. The Hamiltonian of the system can be reduced to

$$H = g_0 \sum_j (\sigma_j^\dagger \sigma_{j+1} + \sigma_j^\dagger \sigma_{j-1}) + \sum_n nF [1 + K \cos(F_D t + \varphi)] \sigma_n^\dagger \sigma_n. \quad (\text{D2})$$

We treat the second term as the free Hamiltonian $H_0(t)$ satisfying the commutation relation $[H_0(t), H_0(t')] = 0$, and the first term is the interacting Hamiltonian, H_I . Thus, the transformation from the Schrödinger interaction to the interaction picture is expressed as

$$\sigma_n \rightarrow e^{-inF \int_0^t d\tau [1 + K \cos(F_D \tau + \varphi)]} \sigma_n = e^{-inFt + in \frac{KF}{F_D} \sin(\varphi) - in \frac{KF}{F_D} \sin(F_D t + \varphi)} \sigma_n. \quad (\text{D3})$$

Then, the interaction-picture Hamiltonian is

$$H_{int}(t) = g_1 \sum_j \sigma_j^\dagger \sigma_{j+1} e^{-iFt - i \frac{KF}{F_D} \sin(F_D t + \varphi)} + \text{H.c.}, \quad (\text{D4})$$

where $g_1 = g_0 e^{i \frac{KF}{F_D} \sin(\varphi)}$. Using the expansion $e^{ia \sin(t)} = \sum_{\mu=-\infty}^{\infty} J_\mu(a) e^{i\mu t}$, in which J_μ is the μ th-order Bessel

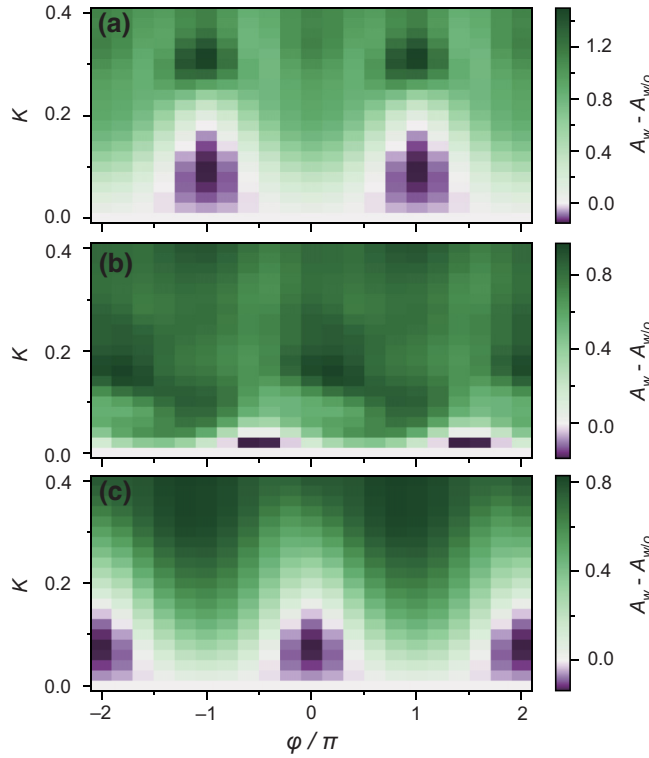


FIG. 9. The theoretical localization data of the super-Bloch oscillations. The differences of the average amplitude with driving (A_w) and without driving ($A_{w/o}$) versus the driving amplitude K and the initial driving phase φ , with $F/2\pi = 20$ MHz: (a) $F_D = 22$ MHz; (b) $F_D = 20$ MHz; and (c) $F_D = 18$ MHz.

function, the above Hamiltonian can be rewritten as

$$H_{int}(t) = \sum_j \sigma_j^\dagger \sigma_{j+1} \sum_\mu g_{\text{eff},\mu} e^{-i(F-\mu F_D)t} + \text{H.c.}, \quad (\text{D5})$$

where the effective coupling strength reads

$$\begin{aligned} g_{\text{eff},\mu} &= g_1 e^{i\mu\varphi} J_\mu \left(-\frac{KF}{F_D} \right) \\ &= g_0 e^{i\frac{KF}{F_D} \sin(\varphi) + i\mu\varphi} J_\mu \left(-\frac{KF}{F_D} \right). \end{aligned} \quad (\text{D6})$$

In the case of $F \approx F_D$ as in the experiment, all terms except $\mu = 1$ have a phase that rotates quickly. We can formally keep only the contribution of $\mu = 1$ (the main cause of SBO) and $\mu = 0$ (BO), assuming a coarse-grained temporal resolution greater than $1/(F + F_D)$. That is,

$$H_{int}(t) = \sum_j \sigma_j^\dagger \sigma_{j+1} (g_{\text{eff},0} e^{-iFt} + g_{\text{eff},1} e^{-i(F-F_D)t}) + \text{H.c.} \quad (\text{D7})$$

Therefore, here are two conclusions,

- (1) Recall that $J_0(0) = 1$ and $J_1(0) = 0$. Thus, if $K \ll 1$, we have $g_{\text{eff},0} \gg g_{\text{eff},1}$, so that SBO is not visible.
- (2) The frequency of SBO is $\nu_S = F - F_D$. In Fig. 3(b), we show $F = F_D$. In this case, the excitation can propagate to infinitely far away.

-
- [1] F. Bloch, Über die Quantenmechanik der Elektronen in Kristallgittern, *Z. Phys.* **52**, 555 (1929).
 - [2] C. Zener, A theory of the electrical breakdown of solid dielectrics, *Proc. R. Soc. Lond. Ser. A* **145**, 523 (1934).
 - [3] G. H. Wannier, Wave functions and effective Hamiltonian for Bloch electrons in an electric field, *Phys. Rev.* **117**, 432 (1960).
 - [4] K. Leo, P. H. Bolivar, F. Brüggemann, R. Schwedler, and K. Köhler, Observation of Bloch oscillations in a semiconductor superlattice, *Solid State Commun.* **84**, 943 (1992).
 - [5] J. Feldmann, K. Leo, J. Shah, D. A. Miller, J. Cunningham, T. Meier, G. Von Plessen, A. Schulze, P. Thomas, and S. Schmitt-Rink, Optical investigation of Bloch oscillations in a semiconductor superlattice, *Phys. Rev. B* **46**, 7252 (1992).
 - [6] M. B. Dahan, E. Peik, J. Reichel, Y. Castin, and C. Salomon, Bloch oscillations of atoms in an optical potential, *Phys. Rev. Lett.* **76**, 4508 (1996).
 - [7] S. Wilkinson, C. Bharucha, K. Madison, Q. Niu, and M. Raizen, Observation of atomic Wannier-Stark ladders in an accelerating optical potential, *Phys. Rev. Lett.* **76**, 4512 (1996).
 - [8] B. P. Anderson and M. A. Kasevich, Macroscopic quantum interference from atomic tunnel arrays, *Science* **282**, 1686 (1998).
 - [9] R. Morandotti, U. Peschel, J. Aitchison, H. Eisenberg, and Y. Silberberg, Experimental observation of linear and non-linear optical Bloch oscillations, *Phys. Rev. Lett.* **83**, 4756 (1999).
 - [10] X.-Y. Guo, Z.-Y. Ge, H. Li, Z. Wang, Y.-R. Zhang, P. Song, Z. Xiang, X. Song, Y. Jin, and L. Lu, *et al.*, Observation of Bloch oscillations and Wannier-Stark localization on a superconducting quantum processor, *npj Quantum Inf.* **7**, 51 (2021).
 - [11] E. Haller, R. Hart, M. J. Mark, J. G. Danzl, L. Reichsöllner, and H.-C. Nägerl, Inducing transport in a dissipation-free lattice with super Bloch oscillations, *Phys. Rev. Lett.* **104**, 200403 (2010).
 - [12] Q. Thommen, J. C. Garreau, and V. Zehnlé, Theoretical analysis of quantum dynamics in one-dimensional lattices: Wannier-Stark description, *Phys. Rev. A* **65**, 053406 (2002).
 - [13] H. Korsch and S. Mossmann, An algebraic solution of driven single band tight binding dynamics, *Phys. Lett. A* **317**, 54 (2003).
 - [14] T. Hartmann, F. Keck, H. Korsch, and S. Mossmann, Dynamics of Bloch oscillations, *New J. Phys.* **6**, 2 (2004).
 - [15] Q. Thommen, J. C. Garreau, and V. Zehnlé, Atomic motion in tilted optical lattices: An analytical approach, *J. Opt. B: Quantum Semiclassical Opt.* **6**, 301 (2004).
 - [16] A. R. Kolovsky and H. J. Korsch, Dynamics of interacting atoms in driven tilted optical lattices, *ArXiv:0912.2587* (2009).

- [17] Z. Turker and C. Yuce, Super Bloch oscillation in a \mathcal{PT} symmetric system, *Phys. Lett. A* **380**, 2260 (2016).
- [18] A. Pereira, M. L. Lyra, F. A. de Moura, A. R. Neto, and W. Dias, Nonlinear wave-packet dynamics resonantly driven by ac and dc fields, *Commun. Nonlinear Sci. Numerical Simul.* **64**, 89 (2018).
- [19] A. Alberti, V. Ivanov, G. Tino, and G. Ferrari, Engineering the quantum transport of atomic wavefunctions over macroscopic distances, *Nat. Phys.* **5**, 547 (2009).
- [20] V. Ivanov, A. Alberti, M. Schioppo, G. Ferrari, M. Artoni, M. Chiofalo, and G. Tino, Coherent delocalization of atomic wave packets in driven lattice potentials, *Phys. Rev. Lett.* **100**, 043602 (2008).
- [21] C. Sias, H. Lignier, Y. Singh, A. Zenesini, D. Ciampini, O. Morsch, and E. Arimondo, Observation of photon-assisted tunneling in optical lattices, *Phys. Rev. Lett.* **100**, 040404 (2008).
- [22] X. Gu, A. F. Kockum, A. Miranowicz, Y.-x. Liu, and F. Nori, Microwave photonics with superconducting quantum circuits, *Phys. Rep.* **718**, 1 (2017).
- [23] A. Blais, A. L. Grimsmo, S. M. Girvin, and A. Wallraff, Circuit quantum electrodynamics, *Rev. Mod. Phys.* **93**, 025005 (2021).
- [24] F. Arute, K. Arya, R. Babbush, D. Bacon, J. C. Bardin, R. Barends, R. Biswas, S. Boixo, F. G. Brandao, and D. A. Buell, *et al.*, Quantum supremacy using a programmable superconducting processor, *Nature* **574**, 505 (2019).
- [25] Y. Wu, W.-S. Bao, S. Cao, F. Chen, M.-C. Chen, X. Chen, T.-H. Chung, H. Deng, Y. Du, and D. Fan, *et al.*, Strong quantum computational advantage using a superconducting quantum processor, *Phys. Rev. Lett.* **127**, 180501 (2021).
- [26] N. Ofek, A. Petrenko, R. Heeres, P. Reinhold, Z. Leghtas, B. Vlastakis, Y. Liu, L. Frunzio, S. Girvin, and L. Jiang, *et al.*, Extending the lifetime of a quantum bit with error correction in superconducting circuits, *Nature* **536**, 441 (2016).
- [27] Y. Y. Gao, B. J. Lester, K. S. Chou, L. Frunzio, M. H. Devoret, L. Jiang, S. Girvin, and R. J. Schoelkopf, Entanglement of bosonic modes through an engineered exchange interaction, *Nature* **566**, 509 (2019).
- [28] H. Paik, D. I. Schuster, L. S. Bishop, G. Kirchmair, G. Catelani, A. P. Sears, B. Johnson, M. Reagor, L. Frunzio, and L. I. Glazman, *et al.*, Observation of high coherence in josephson junction qubits measured in a three-dimensional circuit QED architecture, *Phys. Rev. Lett.* **107**, 240501 (2011).
- [29] R. Barends, J. Kelly, A. Megrant, D. Sank, E. Jeffrey, Y. Chen, Y. Yin, B. Chiaro, J. Mutus, and C. Neill, *et al.*, Coherent Josephson qubit suitable for scalable quantum integrated circuits, *Phys. Rev. Lett.* **111**, 080502 (2013).
- [30] E. Jeffrey, D. Sank, J. Mutus, T. White, J. Kelly, R. Barends, Y. Chen, Z. Chen, B. Chiaro, and A. Dunsworth, *et al.*, Fast accurate state measurement with superconducting qubits, *Phys. Rev. Lett.* **112**, 190504 (2014).
- [31] Z. Yan, Y.-R. Zhang, M. Gong, Y. Wu, Y. Zheng, S. Li, C. Wang, F. Liang, J. Lin, and Y. Xu, *et al.*, Strongly correlated quantum walks with a 12-qubit superconducting processor, *Science* **364**, 753 (2019).
- [32] L. Zhou, S. Yang, Y.-X. Liu, C. Sun, and F. Nori, Quantum Zeno switch for single-photon coherent transport, *Phys. Rev. A* **80**, 062109 (2009).
- [33] X. Guo, H. Deng, H. Li, P. Song, Z. Wang, L. Su, J. Li, Y. Jin, and D. Zheng, Modulation of energy spectrum and control of coherent microwave transmission at single-photon level by longitudinal field in a superconducting quantum circuit, *Chin. Phys. B* **27**, 074206 (2018).
- [34] Y. Wu, L.-P. Yang, M. Gong, Y. Zheng, H. Deng, Z. Yan, Y. Zhao, K. Huang, A. D. Castellano, and W. J. Munro, *et al.*, An efficient and compact switch for quantum circuits, *npj Quantum Inf.* **4**, 50 (2018).
- [35] G. Dolan, Offset masks for lift-off photoprocessing, *Appl. Phys. Lett.* **31**, 337 (1977).
- [36] J. S. Kelly, *Fault-Tolerant Superconducting Qubits* (University of California, Santa Barbara, California, 2015).
- [37] Z. Chen, A. Megrant, J. Kelly, R. Barends, J. Bochmann, Y. Chen, B. Chiaro, A. Dunsworth, E. Jeffrey, and J. Mutus, *et al.*, Fabrication and characterization of aluminum airbridges for superconducting microwave circuits, *Appl. Phys. Lett.* **104**, 052602 (2014).
- [38] R. Barends, J. Kelly, A. Megrant, A. Veitia, D. Sank, E. Jeffrey, T. C. White, J. Mutus, A. G. Fowler, and B. Campbell, *et al.*, Superconducting quantum circuits at the surface code threshold for fault tolerance, *Nature* **508**, 500 (2014).
- [39] J. Koch, M. Y. Terri, J. Gambetta, A. A. Houck, D. I. Schuster, J. Majer, A. Blais, M. H. Devoret, S. M. Girvin, and R. J. Schoelkopf, Charge-insensitive qubit design derived from the Cooper pair box, *Phys. Rev. A* **76**, 042319 (2007).